Electronic modulation of sprout-shaped NiCoP nanoarrays by N and Ce doping for efficient overall water splitting

Ting Zhao[1], Guancheng Xu[1] (✉), Bingbing Gong[2], Jiahui Jiang[1], and Li Zhang[1,2] (✉)

[1] State Key Laboratory of Chemistry and Utilization of Carbon Based Energy Resources, College of Chemistry, Xinjiang University, Urumqi 830017, China
[2] College of Chemical Engineering, Xinjiang University, Urumqi 830017, China

ABSTRACT

Bifunctional catalysts for hydrogen/oxygen evolution reactions (HER/OER) are urgently needed given the bright future of water splitting hydrogen production technology. Here, the self-supporting N and Ce dual-doped NiCoP nanoarrays (denoted N,Ce-NiCoP/NF) grown on Ni foam are successfully constructed. When the N,Ce-NiCoP/NF simultaneously acts as the HER and OER electrodes, the voltages of 1.54 and 2.14 V are obtained for driving 10 and 500 mA·cm⁻² with a robust durability, and demonstrate its significant potential for practical water electrolysis. According to both experiments and calculations, the electronic structure of NiCoP may be significantly altered by strategically incorporating N and Ce into the lattice, which in turn optimizes the Gibbs free energy of HER/OER intermediates and speeds up the water splitting kinetics. Moreover, the sprout-shaped morphology significantly increases the exposure of active sites and facilitates charge/mass transfer, thereby augmenting catalyst performance. This study offers a potentially effective approach involving the regulation of anion and cation double doping, as well as architectural engineering, for the purpose of designing and optimizing innovative electrocatalysts.

KEYWORDS

transition metal phosphides, overall water splitting, elements doping, nanoarrays

1   Introduction

The replacement of existing fossil fuels with electrolyzed hydrogen (H_2) of high purity may significantly solve energy and environmental issues [1, 2]. Until recently, the most advanced electrocatalysts for hydrogen evolution reaction (HER) and oxygen evolution reaction (OER) are still Pt-based and Ru/Ir materials [3–5]. However, inadequate reserves, high cost, and short lifespan restrict the practical use of such catalysts, and there is an immediate need to produce earth-abundant bifunctional electrocatalysts with excellent water splitting performance.

Thanks to their various electron orbitals, metallic characteristics, and inexpensive cost, transition metal phosphides (TMPs) have been researched extensively in this area [6, 7]. Increased conductivity and a synergistic effect between components provide bimetallic phosphides (NiCoP [8, 9], CoMoP [10], NiFeP [11], etc.) superior electrocatalytic activity compared to monometallic phosphides. Although some remarkable progress has been made, its catalytic performance and stability are still difficult to meet the requirements of industrial applications. Studies in the last several years have demonstrated that heteroatom doping engineering is not only easy to implement, but also has the potential to modify the electronic structure, reduce the reaction energy barrier, speed up reaction kinetics, and fundamentally increase intrinsic activity [12, 13]. So far, research has documented doping TMPs with different d-block metals (such as Mo [14], Cu [15], Fe [16], Mn [17], etc.) to boost their water-splitting activity. However, investigations on doping TMPs with

f-block metals are few. Due to its comparable electronic structure to alkali metals, the f-block metal contributes to increased catalytic activity by creating oxygen vacancies [18]. When coupled with other active catalysts, Ce as a rare earth metal with distinctive 4f electrons, may considerably increase the catalytic efficiency [19–21]. In particular, the mixed electronic/ionic conductivity seen in Ce-related compounds is the result of the tunable transition between Ce^{3+} and Ce^{4+}, which may make several active sites for mobile oxygen accessible, thus boosting electrocatalytic activity [22, 23]. Relatively recently, Liu et al. [18] reported that Ce doping generated a favorable oxidation transition at the active site, which was beneficial to OER activity of NiFe-based hydroxide catalysts. Furthermore, N is often regarded as a good anionic dopant due to its high electronegativity, which may boost catalytic performance by improving electron donor characteristics and conductivity [24]. Zhou et al. [25] discovered that adding N to the Ni_5P_4 lattice may drastically increase the active sites of material and alter its electronic structure, both of which would lead to a lower free energy of adsorption for hydrogen. Notably, ion double-doped electrocatalysts for water splitting are rare, although single anion or cation doped ones are ubiquitous.

In light of the aforementioned considerations, we report N and Ce dual-doped NiCoP/CoP directly grown on Ni foam (denoted N,Ce-NiCoP/NF) using a straightforward two-step technique. Using the hydrothermal technique, a nanoneedle array of Ce-NiCo precursor was formed on NF. Next, N,Ce-NiCoP/NF with a morphology similar to that of sprouts was created by treating the

Address correspondence to Guancheng Xu, xuguancheng@xju.edu.cn; Li Zhang, zhangli420@xju.edu.cn

precursor with simultaneous nitrogen doping and phosphating. As a result, N,Ce-NiCoP/NF electrode requires a low potentials of 78 and 212 mV to afford 10 mA·cm^{-2} for HER and OER, respectively. Furthermore, for total water splitting using N,Ce-NiCoP/NF acting as both anode and cathode catalysts, the cell potential was only 1.54 V for a current density of 10 mA·cm^{-2}, with high durability of around 100 h. Experiments and density functional theory (DFT) calculations results showed that N and Ce doping improved the kinetics of the HER/OER processes by increasing the intrinsic catalytic activity of the catalyst and decreasing the adsorption energies of hydrogen-containing and oxygen-containing intermediates (H*, OH*, and OOH*) on the catalyst surface.

2 Results and discussion

The procedure for making N,Ce-NiCoP/NF is shown in Fig. 1. Initially, using hydrothermal technique, the Ce-doped NiCo precursor was first modified onto the Ni foam. The doping level of Ce-cation may be controlled by regulating the amount of cerium(III) nitrate hexahydrate introduced during this process. Subsequently, the Ce-doped NiCo precursor was calcined in an Ar environment using ammonium bicarbonate and sodium hypophosphite as nitrogen and phosphorus sources, respectively, to produce the final N,Ce-NiCoP/NF electrocatalyst. To comprehend the significance of the double doping effect, we produced N and Ce singly doped control samples (designated N-NiCoP/NF and Ce-NiCoP/NF, respectively) and undoped NiCoP/NF.

X-ray diffraction (XRD) was used to determine the phase composition of as-synthesized samples. Figure S1 in the Electronic Supplementary Material (ESM) depicts the NiCo precursor/NF phase. The diffraction patterns resemble those of $Ni_2(OH)_2CO_3$ (PDF#35-0501), the $Co_2(OH)_2CO_3$ (PDF#48-0083), and Ni (PDF#04-0850). The Ce-NiCo precursor/NF has similar diffraction to NiCo precursor/NF, and no peaks belonging to Ce species were identified. Therefore, Ce doping modification has little effect on the phase and crystal structure of the materials. After simultaneous nitrogen doping and phosphating treatment, N,Ce-NiCoP/NF (Fig. 2(a)) shows diffraction peaks at 30.7°, 40.8°, 47.3°, and 54.2° corresponding to the (110), (111), (210), and (300) crystal planes of NiCoP (PDF#71-2336), respectively. The other distinct diffraction peaks located at 31.7°, 36.1°, and 48.1° are assigned to the (011), (102), and (211) crystalline planes of CoP (PDF#89-2598), respectively. The three prominent peaks denoted by "*" are from the Ni foam substrate. Notably, the lack of typical peaks for Ce-based compounds and nitrides in the XRD patterns indicates that the dual-doping of cerium and nitrogen has not resulted in the formation of a new crystal phase in the catalyst. Ce-

NiCoP/NF and N-NiCoP/NF have comparable diffraction peaks with NiCoP/NF, lending more credence to this concept. The XRD peaks of N,Ce-NiCoP/NF were slightly displaced to higher angles compared to those of undoped NiCoP/NF due to the difference in ionic radii between the dopants and the host [26]. Scanning electron microscopy (SEM) was used to investigate the surface morphology of catalysts. The nanoneedle-like NiCo precursor was uniformly grown on the Ni foam (Figs. S2(a)–S2(c) in the ESM). After Ce was introduced, the SEM images of Ce-NiCo precursor (Figs. S2(d)–S2(f) in the ESM) show nanoneedles structure with reduced diameter. N,Ce-NiCoP takes on a distinctive sprout-shaped structure on the NF substrate (Fig. 2(c) and Figs. S2(g)–S2(i) in the ESM) with a clearly delineated "pillar" and "tip" component after Ce-NiCo precursor undergoes simultaneous nitrogen doping and phosphating treatments. The unique sprout-shaped structure provides a multitude of active sites and an easily accessible vast surface area, both of which increase the rate of diffusion of electrolyte and facilitate the release of bubbles [27]. To explore the reason for the formation of this special morphology, undoped NiCoP/NF and singly doped NiCoP/NF were examined by SEM. Only N-NiCoP/NF exhibits the distinctive sprout shape (Fig. S3 in the ESM), suggesting that N doping is pivotal in the development of this morphology. The transmission electron microscopy (TEM) picture reveals further information on the structure of a single N,Ce-NiCoP/NF. Figure 2(d) shows that the sprout-shaped N,Ce-NiCoP/NF is made up of a lot of irregular spherical particles and an amorphous layer around 28 nm thick. When exposed to air, surface phosphide may be partially oxidized to phosphate, which can then contribute to the formation of the amorphous layer [28]. The high-resolution TEM (HRTEM) image of N,Ce-NiCoP/NF (Fig. 2(e) and Fig. S4 in the ESM) shows three lattice fringes of 0.170, 0.222, and 0.203 nm, which correspond to the (300) and (111) planes of NiCoP and the (112) plane of CoP [29, 30]. In addition, selected area electron diffraction (SAED) pattern also supports the TEM results (Fig. S5 in the ESM). The energy-dispersive X-ray (EDX) elemental mapping images (Figs. 2(f)–2(l)) show that N, Ce, Ni, Co, P, and O are evenly dispersed on sprout-shaped N,Ce-NiCoP/NF. The aforementioned findings demonstrate that nitrogen anions and cerium cations have been effectively doped into NiCoP. The source of O element in N,Ce-NiCoP/NF comes from the process of synthesizing the catalyst in addition to the oxidation in the exposed air. Specifically, on the one hand, the O element present in N,Ce-NiCoP/NF may potentially stem from the amorphous shell on the surface. This amorphous shell can be attributed to the phosphate component due to the inevitable surface oxidation of the electrocatalyst upon exposure to air [31–33]. On the other hand, during the heat treatment process, with the increase of temperature,
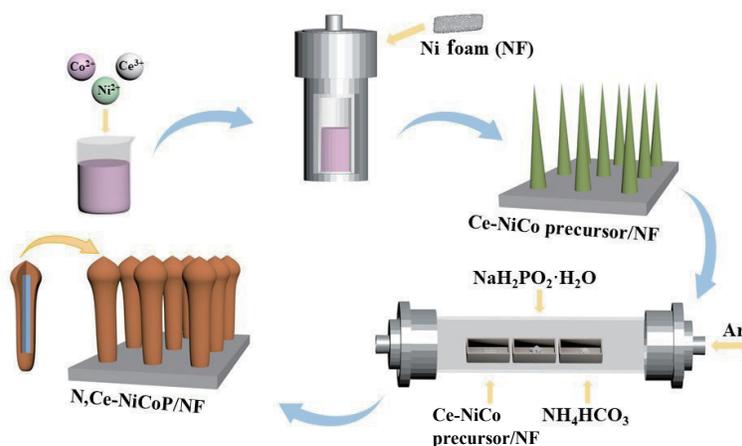

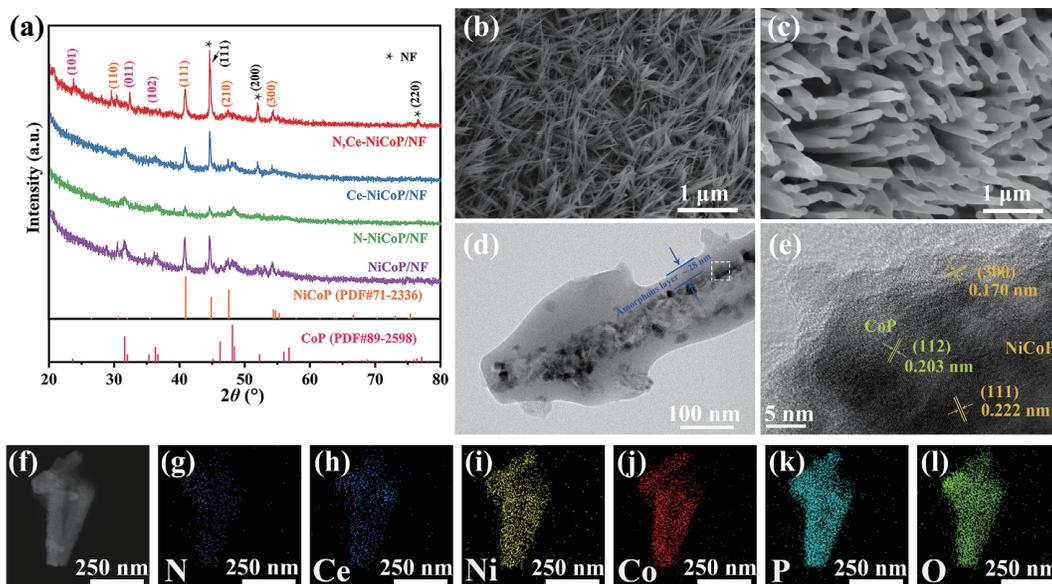**Figure 1** Schematic illustration of the synthesis of N,Ce-NiCoP/NF.

Figure 2 (a) XRD patterns of NiCoP/NF, N-NiCoP/NF, Ce-NiCoP/NF, and N,Ce-NiCoP/NF. (b) SEM image of Ce-NiCo precursor/NF. (c) SEM image, (d) and (e) TEM images, and (f)–(l) EDX mapping images of N,Ce-NiCoP/NF.

$NaH_2PO_2 \cdot H_2O$ is decomposed into PH_3 and H_2O vapor, and water vapor accelerates the oxidation of phosphide, so the O element is also introduced in the synthesis process [28]. Besides, the EDX mapping images of other as-prepared samples show that the elements are uniformly distributed (Figs. S6–S8 in the ESM). Note that the O content in NiCoP/NF is significantly lower than the other as-prepared samples, suggesting that the introduction of N and Ce into NiCoP may promote phosphate formation. The phosphate layer may enhance the active sites of the catalyst and also serve as a passivation layer, inhibiting the further dissolution of TMPs and enhancing the stability of the catalyst [26].

Figure 3 displays the results of X-ray photoelectron spectroscopy (XPS) tests used to determine the chemical make-up of the samples and the valence changes of the elements before and after nitrogen and cerium doping. Figure 3(a) shows that the survey spectra corroborate the existence of N, Ce, Ni, Co, P, and O elements in N,Ce-NiCoP/NF as well as the element compositions in control samples. Three peaks at 897.59, 885.21, and 904.1 eV are allocated to Ce^{3+} in the Ce 3d spectra of N,Ce-NiCoP/NF shown in Fig. 3(b), while five peaks at 904.98, 901.27, 893.71, 887.52, and 882.27 eV are attributed to Ce^{4+} [34]. Electron paramagnetic resonance (EPR) further confirms that the presence of Ce^{3+} and Ce^{4+} would result in abundant oxygen vacancy defects. The signal of $g = 2.004$ in EPR demonstrates oxygen vacancy flaws in the structure, as seen in Fig. S9 in the ESM [35]. High oxygen vacancy densities have been shown to improve OER catalytic performance, since they dramatically speed up electrical conductivity and surface redox kinetics [36]. When comparing Ce-NiCoP/NF and N,Ce-NiCoP/NF, it is notable that the binding energies of the Ce species in the latter are positively shifted by about 0.6 eV, showing that the N-doping brought the modified local electronic structure of Ce and induced the electronic interaction, which was favorable for enhancing electrocatalytic activity. In the high-resolution Ni 2p region of N,Ce-NiCoP/NF (Fig. 3(c)), two major peaks associated to $Ni-PO_x$ are concentrated at 873.58 (Ni $2p_{1/2}$) and 856.06 eV (Ni $2p_{3/2}$) [37]. Peaks with energies of 880.68 and 861.56 eV correspond to satellite peaks (denoted "Sat."). Two peaks at 869.83 and 852.73 eV were ascribed to the Ni–P bonding of NiCoP. The Co $2p_{3/2}$ peaks at 777.28 and 781.30 eV in the Co 2p spectra (Fig. 3(d)) may be ascribed to Co–P in NiCoP and oxidized Co (Co^{2+}) in $Co-PO_x$ [38]. Peak at 797.37 eV corresponds to Co $2p_{1/2}$,

whereas satellite peaks at 785.24 eV and 802.72 eV relate to Co^{2+} species [39, 40]. The P 2p for N,Ce-NiCoP/NF shows two peaks at 129.74 and 133.64 eV, respectively, for the M–P bond (M = Ni, Co) of phosphide and the P–O of phosphate/phosphite (Fig. 3(e)) [30]. The existence of PO_4^{3-} in N,Ce-NiCoP/NF can also be seen in O 1s (Fig. S10 in the ESM) [41, 42]. Note that the P $2p_{1/2}$ peak of N,Ce-NiCoP/NF is particularly weak. Combined with the TEM results, this can be attributed to phosphate on the surface of N,Ce-NiCoP/NF, which encloses the phosphide almost completely. Interestingly, the presence of N promotes the creation of more phosphate, since both Ce-NiCoP/NF and NiCoP/NF contain an apparent P–M bond. Three peaks can be resolved in the N 1 s spectra of N,Ce-NiCoP/NF (Fig. 3(f)), each of which is attributed to a distinct N doping species. The peak at 399.62 eV can be ascribed to N–M bond (M = Co, Ni), suggesting the successful doping of N-anion [43–45]. By analyzing the binding energy position in detail, we learned that the Ni, Co, P, and O species in N,Ce-NiCoP/NF exhibit a positive shift with regard to that for Ce-NiCoP/NF, but a negative shift with respect to that for N-NiCoP/NF. In addition, there is a positive shift in the N binding energies in N,Ce-NiCoP/NF compared to N-NiCoP/NF. In XPS, the binding energies are related to electronic transitions from core atomic orbitals. Because of the different chemical environments, there will be slight shifts in the binding energies that are produced [46]. The electronegativity of N is greater than that of Ce, Ni, Co, and P. Because of this, the atoms of Ce, Ni, Co, and P in Ce-NiCoP/NF have a greater number of electrons than those in N,Ce-NiCoP/NF, which results in lower values for the binding energy. In accordance with the study shown above, the peaks in the Ni, Co, N, and P regions of the N-NiCoP/NF spectra exhibit positive changes in the binding energies compared with N,Ce-NiCoP/NF.

To begin with, the standard experimental calibrations of Hg/HgO in a three-electrode system were conducted (Fig. S11 in the ESM). Furthermore, the optimal doping level of N,Ce-NiCoP/NF was first examined (Figs. S12(a) and S12(b) in the ESM), where it was confirmed that the sample supplemented with 0.130 g $Ce(NO_3)_3 \cdot 6H_2O$ and 0.225 g NH_4HCO_3 showed the highest HER activity. We also synthesized N-NiCoP/NF, Ce-NiCoP/NF, and NiCoP/NF to use as references when studying the effect of anion–cation dual-doping. Compared to NiCoP/NF, N or Ce-modified catalysts have much higher HER activity (Fig. 4(a)). Figure 4(b) compares these catalyst overpotentials at various
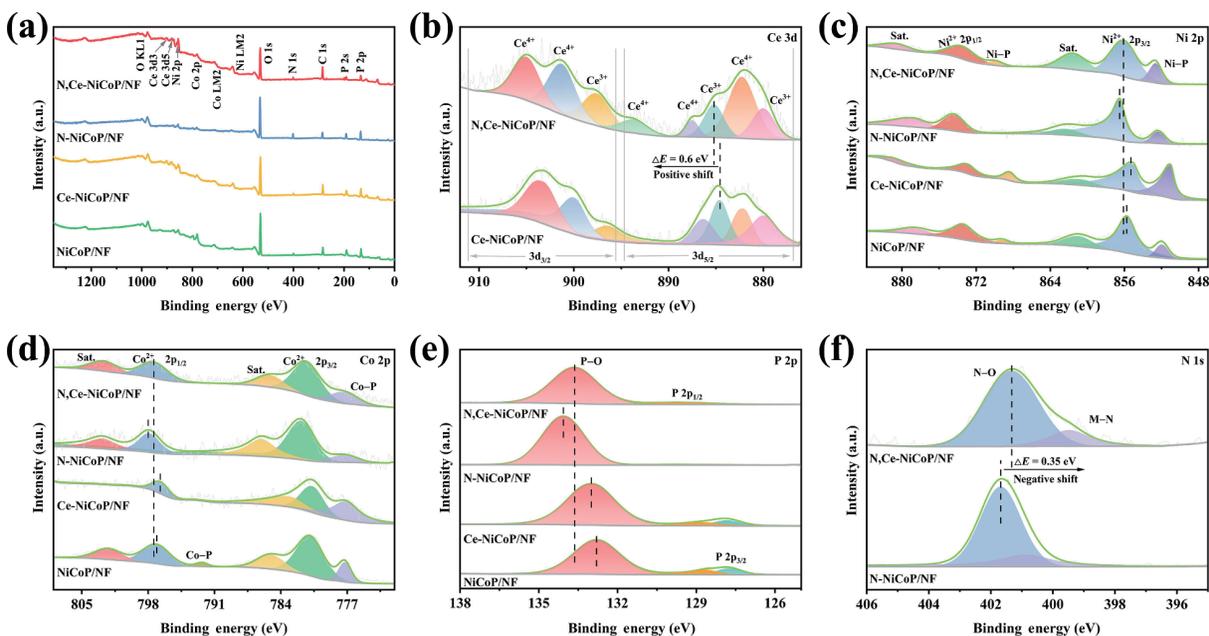
Figure 3 XPS spectra of NiCoP/NF, N-NiCoP/NF, Ce-NiCoP/NF, and N,Ce-NiCoP/NF: (a) survey spectra, (b) Ce 3d, (c) Ni 2p, (d) Co 2p, (e) P 2p, and (f) N 1s.
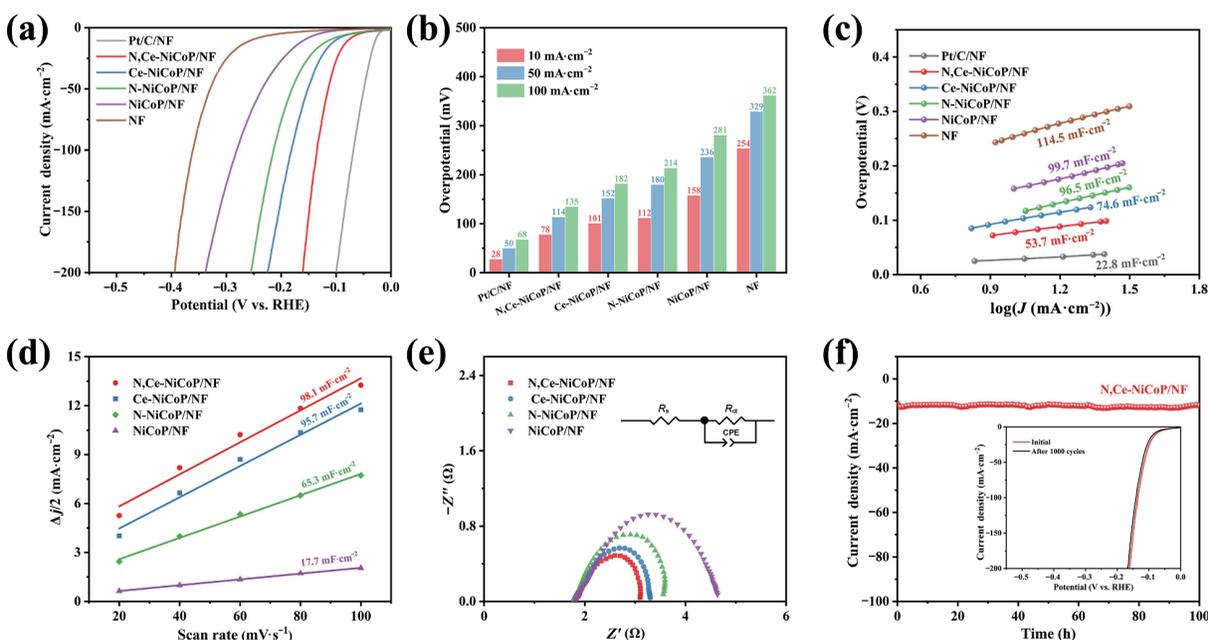

Figure 4 The HER performance of different samples measured in 1 M KOH. (a) Polarization curves. (b) Overpotential at different current densities. (c) Tafel slopes. (d) C_{dl}. (e) Nyquist plots. (f) The stability test of N,Ce-NiCoP/NF at a static overpotential of 78 mV vs. reversible hydrogen electrode (RHE) for 100 h and polarization curves before and after 1000 CV cycles.

current densities. Obviously, N,Ce-NiCoP/NF needs just a relatively low overpotential of 78 mV to give a current density of 10 mA·cm^{-2}, which is significantly better than Ce-NiCoP/NF (101 mV), N-NiCoP (112 mV), NiCoP (158 mV), or NF (254 mV). Also, the overpotentials for N,Ce-NiCoP/NF at current densities of 100 and 500 mA·cm^{-2} are only 135 and 265 mV, respectively (Fig. S13 in the ESM). Such high HER activity surpasses most TMP-based HER catalysts and is fairly close to commercial Pt/C/NF catalyst (Table S1 in the ESM). Figure 4(c) further shows that the Tafel slopes are fitted to be 99.7, 96.5, 74.6, and 53.7 mV·dec^{-1} for NiCoP/NF, N-NiCoP/NF, Ce-NiCoP/NF, and N,Ce-NiCoP/NF, respectively, suggesting the most favorable HER kinetics on N,Ce-NiCoP/NF surface. Moreover, a Volmer–Heyrovsky mechanism (M + H$_2$O + e$^-$ → M–H$_{ads}$ + OH$^-$, M–H$_{ads}$ + H$_2$O + e$^-$ → M + H$_2$ + OH$^-$) is suggested by the Tafel slope of N,Ce-NiCoP/NF, which describes the catalytic HER process [46]. Furthermore, the double-layer capacitances (C_{dl})

determined from the cyclic voltammetry (CV) curves in Figs. S12(c)–S12(f) are shown in Fig. 4(d). The C_{dl} of N,Ce-NiCoP/NF and Ce-NiCoP/NF is as high as 98.1 and 95.7 mF·cm^{-2}, respectively, while the C_{dl} of remaining samples is below 70 mF·cm^{-2}. Since the C_{dl} is proportional to electrochemical active surface area (ECSA), the highest C_{dl} is achieved by N,Ce-NiCoP/NF thanks to its unique sprout-shaped structure and the doping effects of N and Ce dopants. Additionally, charge transfer resistance (R_{ct}) is lower after doping, as shown in the Nyquist plots of electrochemical impedance spectroscopy (EIS) (Fig. 4(e)). N,Ce-NiCoP/NF had the lowest R_{ct}, indicating that it had the quickest charge transfer property, hence enhancing HER performance.

The long-term stability of electrocatalyst is an essential criterion for determining its suitability for large-scale and industrial water electrolysis. In order to learn more about the stability of N,Ce-NiCoP/NF catalyst toward HER, we performed CV cycles and the I–t test technique. As shown in Fig. 4(f), after 1000 CV cycles,

there is almost no change in the current densities, demonstrating exceptional structural stability. Additionally, *I*–*t* measurement was performed to probe the long-term stability of N,Ce-NiCoP/NF. N,Ce-NiCoP/NF was able to maintain HER activity for up to 100 h, as demonstrated in Fig. 4(f). Hydrogen bubbles releasing might be the source of the minor activity oscillation.

The SEM (Fig. S14 in the ESM), XRD (Fig. S15 in the ESM), and XPS (Fig. S16 in the ESM) were performed to disclose the morphology, chemical structure, and surface chemical state of the electrocatalyst after the HER stability test to further understand the HER mechanism of N,Ce-NiCoP/NF. Following the stability examination, the catalyst retained its original morphology and structure (Fig. S14 in the ESM). Moreover, many additional nanosheets were generated on the surface of each nanorod, which may result from hydroxides formation in the alkaline solution [47, 48]. In addition, the phase composition and chemical valence states of N,Ce-NiCoP/NF have been well retained following the durability test, further indicating that N,Ce-NiCoP/NF has exceptional long-term stability for HER.

In addition, OER testing was conducted on the aforementioned catalysts to evaluate their catalytic capabilities. Similarly, the optimum conditions were also investigated (Figs. S17(a) and S17(b) in the ESM) and samples with the same doping level as HER were found to have the best catalytic activity for OER. Figure 5(a) presents the linear sweep voltammetry (LSV) curves of RuO$_2$/NF, NiCoP/NF, N-NiCoP/NF, Ce-NiCoP/NF, and N,Ce-NiCoP/NF. As predicted, N,Ce-NiCoP/NF has excellent catalytic activity with the lowest OER overpotential of 212 mV at 10 mA·cm^{-2} as compared to other electrocatalysts (Fig. 5(b)). Additionally, to drive 100 and 500 mA·cm^{-2}, the N,Ce-NiCoP/NF requires overpotentials of 280 and 360 mV, respectively (Fig. S18 in the ESM). The OER activity of N,Ce-NiCoP/NF exceeds most previously published catalysts for TMPs (Table S2 in the ESM). Tafel slope plots further demonstrate the OER kinetics of catalysts (Fig. 5(b)). Dual-doping facilitates OER kinetics, since N,Ce-NiCoP/NF has the smallest Tafel slope (52.3 mV·dec^{-1}). Measurements of the CV were carried out, so that the ECSA could be approximated (Figs. S17(c)–S17(f) in the ESM and Fig. 5(d)). N,Ce-NiCoP/NF has the highest C_{dl} value of all of the catalysts, coming in at 26.1 mF·cm^{-2}, which means that it has the highest

ECSA. This may be because its active sites are more exposed. The EIS may tell more about the OER kinetics of N,Ce-NiCoP/NF, as illustrated in Fig. 5(e). When compared to other catalysts, N,Ce-NiCoP/NF has a tiny R_{ct} (R_{ct} = 1.4 Ω), much like the EIS spectra of HER. This improvement in the electric conductivity expedites charge transfer, thereby improving the reaction kinetics, which is beneficial to obtaining superior catalytic activity.

The longevity of electrocatalyst is critical for long-term OER operation. Figure 5(f) presents the polarization curves of N,Ce-NiCoP/NF before and after 1000 cycles, and the LSV curves closely overlap. Besides, Fig. 5(f) demonstrates that N,Ce-NiCoP/NF maintained its OER activity for up to 100 h. These results indicate that the prepared N,Ce-NiCoP/NF exhibits excellent electrochemical stability.

Similarly, the N,Ce-NiCoP/NF electrode was characterized using XRD, XPS, and SEM after the OER stability test, as shown in Figs. S15, S16, and S19 in the ESM, respectively. The diffraction peaks of post-N,Ce-NiCoP/NF were assigned to NiCoP and CoP, verifying that the N,Ce-NiCoP/NF electrode has good structural stability. Data from XPS (Fig. S16 in the ESM) shows that the OER test resulted in the Co and Ni species being converted to the higher oxidation state of CoOOH and NiOOH [42, 49–51]. In contrast to the loss of P observed by other studies following OER, our samples still exhibit P 2p peaks with a PO$_4^{3-}$ peak, demonstrating that the shell of phosphate stabilizes the catalyst (Fig. S16(e) in the ESM). Consequently, the amorphous phosphate shell not only boosted the number of active sites, but also inhibited dissolution of the catalysts during electrochemical experiments. SEM images (Fig. S19 in the ESM) show that the nanorod-like shape of N,Ce-NiCoP/NF is preserved during the OER stability test, and the nanorods are adorned with an abundance of nanosheets, which may be due to the surface of the nanorods being oxidized to generate oxyhydroxides, which accelerated the OER kinetics.

N,Ce-NiCoP/NF was used as the anode and cathode electrodes in a two-electrode electrolyzer device in 1 M KOH to determine its bifunctional electrocatalytic activity for water splitting. The N,Ce-NiCoP/NF||N,Ce-NiCoP/NF exhibits remarkable catalytic performance, requiring only 1.54 and 2.14 V to reach 10 and 500 mA·cm^{-2}, respectively (Fig. 6(a)). This not only surpasses the
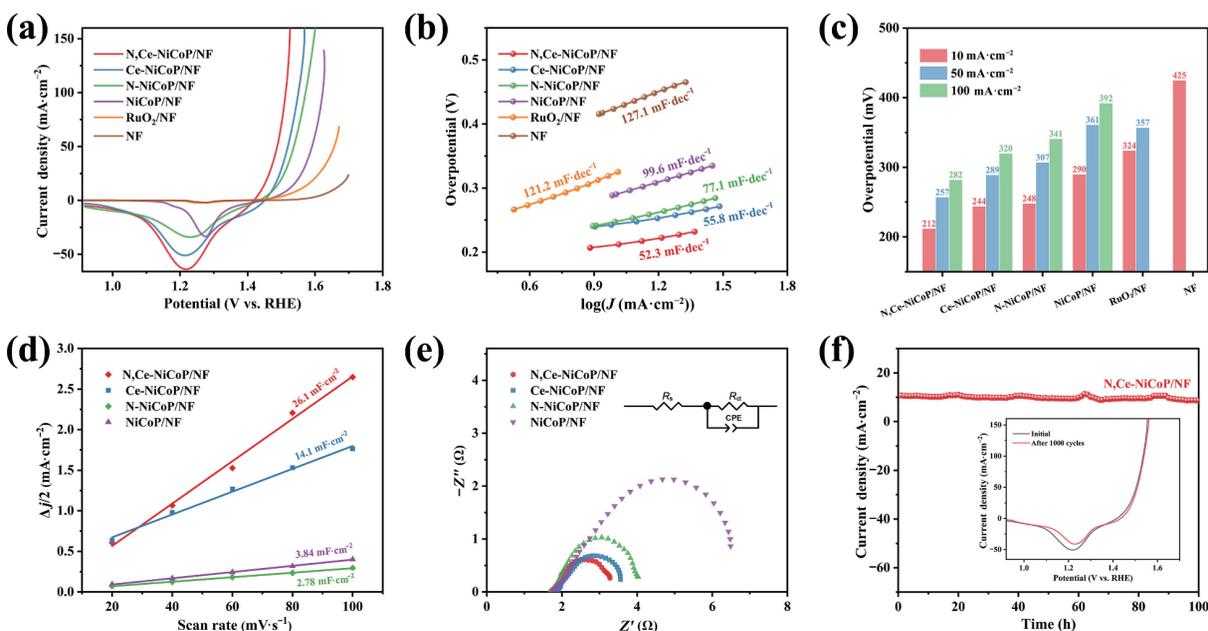
Figure 5 OER electrocatalytic performance of different samples measured in 1 M KOH. (a) Polarization curves. (b) Overpotential at different current densities. (c) Tafel slopes. (d) C_{dl}. (e) Nyquist plots. (f) The stability test of N,Ce-NiCoP/NF at a static overpotential of 212 mV vs. RHE for 100 h and polarization curves before and after 1000 CV cycles.

commercial RuO₂/NF||Pt/C/NF couple, but also outperforms most previously reported TMPs catalysts (Table S3 in the ESM). Additionally, the drainage technique was also used to gather the amounts of H₂ and O₂ produced in the water splitting process as a whole. The volume ratio of H₂ to O₂ is around 2:1, as shown in Fig. 6(b). This suggests that the Faraday efficiency is really close to 100%. Furthermore, the long-term durability of electrocatalyst for overall water splitting at varying current densities was assessed (Fig. 6(c)). After 100 h, the N,Ce-NiCoP/NF||N,Ce-NiCoP/NF electrode changed only marginally at both low and high current densities, demonstrating the outstanding durability. This holds tremendous promise for meeting the needs of commercially applicable applications.

DFT calculation was performed to look into the impact of N-doping and Ce-doping on the electrocatalytic activity of N,Ce-NiCoP. Figure S20 in the ESM shows the optimized structures of those samples. To identify the Ce-doping site, the formation energies of Ce substituted Ni sites (Ce-NiCoP-Ni) and Ce substituted Co sites (Ce-NiCoP-Co) were calculated, which were −0.52 and −0.14 eV, respectively, suggesting that Ce dopants were likely to replace the Ni sites [52].

The free energy of adsorption H (ΔG_{H^*}) is often used to characterize HER activity. A catalyst with the ΔG_{H^*} value that is close to zero is thought to be an excellent candidate for catalyzing the HER process becase it can complete the hydrogen release and proton/electron transfers in a shorter amount of time [41–53]. Figure 7(a) and Fig. S21 in the ESM illustrate the calculated ΔG_{H^*} values for the NiCoP, N-NiCoP, Ce-NiCoP, and N,Ce-NiCoP models, which are 0.24, 0.21, 0.13, and 0.06 eV, respectively. The value of ΔG_{H^*} for N,Ce-NiCoP is in close proximity to the optimal ΔG_{H^*} (~ 0 eV) of the catalyst–H* state. This indicates that the catalyst has a lower energy barrier for the adsorption of H⁺ during the process of HER.

We established optimized models for the adsorption intermediates of NiCoP, N-NiCoP, Ce-NiCoP, and N,Ce-NiCoP (Figs. S22–S25 in the ESM). Figure 7(b) depicts the calculation of the Gibbs free energy for the four phases of the OER at zero voltage. According to the estimated findings, it is evident that the rate-determining steps (RDS) for NiCoP and N-NiCoP were the creation of *OOH, however, following the addition of Ce to NiCoP and N-NiCoP, the RDS is changed to the formation of O₂ [54–56]. Compared to NiCoP (2.38 eV), N-NiCoP (1.89 eV), and Ce-NiCoP (1.74 eV), N,Ce-NiCoP has the lowest RDS energy barrier with 1.70 eV, suggesting that the OER kinetics has been improved after N and Ce doping. This difference in RDS may be due to the NiCoP deformation of the surface structure caused by N and Ce doping. All these findings point to the fact that incorporating N and Ce into NiCoP may significantly improve the thermodynamic behavior of HER and OER processes by altering the electronic structure and chemisorption of phosphides.

Experiment and theory results show that the synergistic effect of the following aspects contributes to the good catalytic activity of N,Ce-NiCoP/NF: (i) Avoiding the need for auxiliary binders during the development of bimetallic phosphides on the NF substrate reduces charge transfer resistance. (ii) The unusual sprout-shaped structure provides a number of easily accessible active sites and broad surface area, both of which increase the diffusion rate of electrolyte and the releasing rate of generated H₂ and O₂ bubbles. (iii) The formation of a phosphate layer may enhance the number of active sites on a catalyst, as well as function as a passivation layer to inhibit the dissolution of N,Ce-NiCoP/NF and render the catalyst more stable. (iv) The addition of N and Ce regulates the electronic structure and improves the chemisorption energy of hydrogen and oxygen intermediates, resulting in improved intrinsic catalytic performance with a decreased reaction barrier. As a result of these merits, N,Ce-NiCoP/NF exhibits remarkable catalytic activity.

3 Conclusions

Using a combination of hydrothermal and subsequent simultaneous nitrogen doping and phosphating treatment, a N,Ce-NiCoP/NF catalyst with a unique bean sprouts structure was fabricated. The unique nanoarchitecture and abundance of oxygen vacancies, as well as the doping effect of N and Ce, allow the
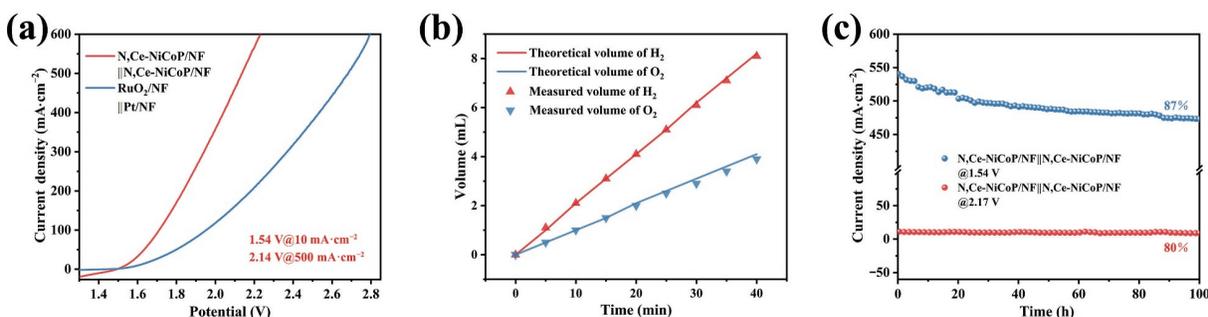

Figure 6 (a) The overall water splitting performance of coupled N,Ce-NiCoP/NF||N,Ce-NiCoP/NF. (b) Comparison of experimental and theoretical amounts of generated gas over 40 min by N,Ce-NiCoP/NF||N,Ce-NiCoP/NF. (c) The stability test of N,Ce-NiCoP/NF||N,Ce-NiCoP/NF at 1.54 and 2.17 V for 100 h.
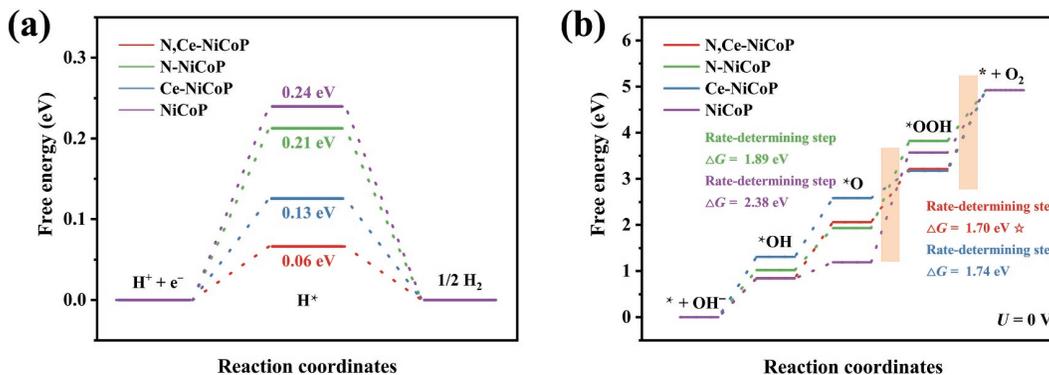

Figure 7 Gibbs free-energy diagrams for (a) HER and (b) OER on NiCoP, Ce-NiCoP, N-NiCoP, and N,Ce-NiCoP surfaces.

bifunctional N,Ce-NiCoP/NF to exhibit small overpotentials of 78 and 212 mV for HER and OER, respectively, as well as a low cell voltage of 1.54 V at 10 mA·cm^{-2} and excellent long-term stability for water splitting. Based on experimental and DFT calculations, it has been observed that the adsorption energy of intermediates containing hydrogen and oxygen can be optimized by altering the electronic structure of NiCoP active site through the introduction of N and Ce, thereby promoting the HER/OER processes. This study demonstrates a novel approach to producing electrocatalysts with high efficiency for energy conversion technology through the utilization of the heteroatom doping and architectural engineering strategy.

Acknowledgements

Electronic Supplementary Material: Supplementary material (expermental details, the XRD patterns, SEM images, EDX mapping, XPS spectra, LSV polarization curves, and CV curves of as-prepared electrode materials) is available in the online version of this article at https://doi.org/10.1007/s12274-023-5769-9.

References

[1] Riyajuddin, S.; Azmi, K.; Pahuja, M.; Kumar, S.; Maruyama, T.; Bera, C.; Ghosh, K. Super-hydrophilic hierarchical Ni-foam-graphene-carbon nanotubes-Ni$_2$P-CuP$_2$ nano-architecture as efficient electrocatalyst for overall water splitting. *ACS Nano* **2021**, *15*, 5586–5599.

[2] Shifa, T. A.; Yusupov, K.; Solomon, G.; Gradone, A.; Mazzaro, R.; Cattaruzza, E.; Vomiero, A. *In situ*-generated oxide in Sn-doped nickel phosphide enables ultrafast oxygen evolution. *ACS Catal.* **2021**, *11*, 4520–4529.

[3] Wang, D. W.; Li, Q.; Han, C.; Lu, Q. Q.; Xing, Z. C.; Yang, X. R. Atomic and electronic modulation of self-supported nickel-vanadium layered double hydroxide to accelerate water splitting kinetics. *Nat. Commun.* **2019**, *10*, 3899.

[4] Wang, H. M.; Chen, Z. N.; Wu, D. S.; Cao, M. N.; Sun, F. F.; Zhang, H.; You, H. H.; Zhuang, W.; Cao, R. Significantly enhanced overall water splitting performance by partial oxidation of Ir through Au modification in core–shell alloy structure. *J. Am. Chem. Soc.* **2021**, *143*, 4639–4645.

[5] Zhai, P. L.; Xia, M. Y.; Wu, Y. Z.; Zhang, G. H.; Gao, J. F.; Zhang, B.; Cao, S. Y.; Zhang, Y. T.; Li, Z. W.; Fan, Z. Z. et al. Engineering single-atomic ruthenium catalytic sites on defective nickel-iron layered double hydroxide for overall water splitting. *Nat. Commun.* **2021**, *12*, 4587.

[6] Zhang, H. J.; Maijenburg, A. W.; Li, X. P.; Schweizer, S. L.; Wehrspohn, R. B. Bifunctional heterostructured transition metal phosphides for efficient electrochemical water splitting. *Adv. Funct. Mater.* **2020**, *30*, 2003261.

[7] Suryawanshi, U. P.; Ghorpade, U. V.; Lee, D. M.; He, M. R.; Shin, S. W.; Kumar, P. V.; Jang, J. S.; Jung, H. R.; Suryawanshi, M. P.; Kim, J. H. Colloidal Ni$_2$P nanocrystals encapsulated in heteroatom-doped graphene nanosheets: A synergy of 0D@2D heterostructure toward overall water splitting. *Chem. Mater.* **2021**, *33*, 234–245.

[8] Lv, X. D.; Li, X. T.; Yang, C.; Ding, X. Q.; Zhang, Y. F.; Zheng, Y. Z.; Li, S. Q.; Sun, X. N.; Tao, X. Large-size, porous, ultrathin NiCoP nanosheets for efficient electro/photocatalytic water splitting. *Adv. Funct. Mater.* **2020**, *30*, 1910830.

[9] Chen, L.; Song, Y. H.; Liu, Y.; Xu, L.; Qin, J. Q.; Lei, Y. P.; Tang, Y. G. NiCoP nanoleaves array for electrocatalytic alkaline H$_2$ evolution and overall water splitting. *J. Energy Chem.* **2020**, *50*, 395–401.

[10] Tang, W. G.; Zhu, S. L.; Jiang, H.; Liang, Y. Q.; Li, Z. Y.; Wu, S. L.; Cui, Z. D. Self-supporting nanoporous CoMoP electrocatalyst for hydrogen evolution reaction in alkaline solution. *J. Colloid Interface Sci.* **2022**, *625*, 606–613.

[11] Kang, Q. L.; Li, M. Y.; Shi, J. W.; Lu, Q. Y.; Gao, F. A universal strategy for carbon-supported transition metal phosphides as high-performance bifunctional electrocatalysts towards efficient overall water splitting. *ACS Appl. Mater. Interfaces* **2020**, *12*, 19447–19456.

[12] El-Refaei, S. M.; Russo, P. A.; Pinna, N. Recent advances in multimetal and doped transition-metal phosphides for the hydrogen evolution reaction at different pH values. *ACS Appl. Mater. Interfaces* **2021**, *13*, 22077–22097.

[13] Jiao, S. L.; Fu, X. W.; Wang, S. Y.; Zhao, Y. Perfecting electrocatalysts via imperfections: Towards the large-scale deployment of water electrolysis technology. *Energy Environ. Sci.* **2021**, *14*, 1722–1770.

[14] Song, H. R.; Wang, J. S.; Zhang, Z. F.; Shai, X.; Guo, Y. Z. Synergistic balancing hydrogen and hydroxyl adsorption/desorption of nickel sulfide via cation and anion dual-doping for boosting alkaline hydrogen evolution. *Chem. Eng. J.* **2021**, *420*, 129842.

[15] Thiyagarajan, D.; Gao, M. Y.; Sun, L.; Dong, X. C.; Zheng, D. H.; Abdul Wahab, M.; Will, G.; Lin, J. J. Nanoarchitectured porous Cu-CoP nanoplates as electrocatalysts for efficient oxygen evolution reaction. *Chem. Eng. J.* **2022**, *432*, 134303.

[16] Sun, H.; Min, Y. X.; Yang, W. J.; Lian, Y. B.; Lin, L.; Feng, K.; Deng, Z.; Chen, M. Z.; Zhong, J.; Xu, L. et al. Morphological and electronic tuning of Ni$_2$P through iron doping toward highly efficient water splitting. *ACS Catal.* **2019**, *9*, 8882–8892.

[17] Liu, Y. H.; Ran, N.; Ge, R. Y.; Liu, J. J.; Li, W. X.; Chen, Y. Y.; Feng, L. Y.; Che, R. C. Porous Mn-doped cobalt phosphide nanosheets as highly active electrocatalysts for oxygen evolution reaction. *Chem. Eng. J.* **2021**, *425*, 131642.

[18] Liu, J. Y.; Liu, Y.; Mu, X. L.; Jang, H.; Lei, Z. W.; Jiao, S. H.; Yan, P. F.; Kim, M. G.; Cao, R. G. Boosting activity and stability of electrodeposited amorphous Ce-doped NiFe-based catalyst for electrochemical water oxidation. *Adv. Funct. Mater.* **2022**, *32*, 2204086.

[19] Wu, X. X.; Zhang, T.; Wei, J. X.; Feng, P. F.; Yan, X. B.; Tang, Y. Facile synthesis of Co and Ce dual-doped Ni$_3$S$_2$ nanosheets on Ni foam for enhanced oxygen evolution reaction. *Nano Res.* **2020**, *13*, 2130–2135.

[20] Zhong, H. H.; Alberto Estudillo-Wong, L.; Gao, Y.; Feng, Y. J.; Alonso-Vante, N. Oxygen vacancies engineering by coordinating oxygen-buffering CeO$_2$ with CoO nanorods as efficient bifunctional oxygen electrode electrocatalyst. *J. Energy Chem.* **2021**, *59*, 615–625.

[21] Wu, Q.; Gao, Q. P.; Sun, L. M.; Guo, H. M.; Tai, X. S.; Li, D.; Liu, L.; Ling, C. Y.; Sun, X. P. Facilitating active species by decorating CeO$_2$ on Ni$_3$S$_2$ nanosheets for efficient water oxidation electrocatalysis. *Chinese J. Catal.* **2021**, *42*, 482–489.

[22] Zai, S. F.; Gao, X. Y.; Yang, C. C.; Jiang, Q. Ce-modified Ni(OH)$_2$ nanoflowers supported on NiSe$_2$ octahedra nanoparticles as high-efficient oxygen evolution electrocatalyst. *Adv. Energy Mater.* **2021**, *11*, 2101266.

[23] Xu, H. J.; Shan, C. F.; Wu, X. X.; Sun, M. Z.; Huang, B. L.; Tang, Y.; Yan, C. H. Fabrication of layered double hydroxide microcapsules mediated by cerium doping in metal-organic frameworks for boosting water splitting. *Energy Environ. Sci.* **2020**, *13*, 2949–2956.

[24] Zhang, R.; Huang, J.; Chen, G. L.; Chen, W.; Song, C. S.; Li, C. R.; Ostrikov, K. *In situ* engineering bi-metallic phospho-nitride bi-functional electrocatalysts for overall water splitting. *Appl. Catal. B: Environ.* **2019**, *254*, 414–423.

[25] Zhou, G. Y.; Ma, Y. R.; Wu, X. M.; Lin, Y. Z.; Pang, H.; Zhang, M. Y.; Xu, L.; Tian, Z. Q.; Tang, Y. W. Electronic modulation by N incorporation boosts the electrocatalytic performance of urchin-like Ni$_5$P$_4$ hollow microspheres for hydrogen evolution. *Chem. Eng. J.* **2020**, *402*, 126302.

[26] Chang, J. F.; Wang, G. Z.; Yang, Z. Z.; Li, B. Y.; Wang, Q.; Kuliiev, R.; Orlovskaya, N.; Gu, M.; Du, Y. G.; Wang, G. F. et al. Dual-doping and synergism toward high-performance seawater electrolysis. *Adv. Mater.* **2021**, *33*, 2101425.

[27] Kim, D.; Qin, X. Y.; Yan, B. Y.; Piao, Y. Sprout-shaped Mo-doped CoP with maximized hydrophilicity and gas bubble release for high-performance water splitting catalyst. *Chem. Eng. J.* **2021**, *408*, 127331.

[28] He, L.; Gong, L.; Gao, M.; Yang, C. W.; Sheng, G. P. *In situ* formation of NiCoP@phosphate nanocages as an efficient bifunctional electrocatalyst for overall water splitting. *Electrochim. Acta* **2020**, *337*, 135799.

[29] Liu, H.; Ma, X.; Hu, H.; Pan, Y. Y.; Zhao, W. N.; Liu, J. L.; Zhao, X. Y.; Wang, J. L.; Yang, Z. X.; Zhao, Q. S. et al. Robust NiCoP/CoP heterostructures for highly efficient hydrogen evolution electrocatalysis in alkaline solution. *ACS Appl. Mater. Interfaces* **2019**, *11*, 15528–15536.

[30] Boppella, R.; Tan, J.; Yang, W.; Moon, J. Homologous CoP/NiCoP heterostructure on N-doped carbon for highly efficient and pH-universal hydrogen evolution electrocatalysis. *Adv. Funct. Mater.* **2019**, *29*, 1807976.

[31] Hu, E. L.; Ning, J. Q.; Zhao, D.; Xu, C. Y.; Lin, Y. Y.; Zhong, Y. J.; Zhang, Z. Y.; Wang, Y. J.; Hu, Y. A room-temperature postsynthetic ligand exchange strategy to construct mesoporous Fe-doped CoP hollow triangle plate arrays for efficient electrocatalytic water splitting. *Small* **2018**, *14*, 1704233.

[32] Xu, X. J.; Du, P. Y.; Guo, T.; Zhao, B. L.; Wang, H. L.; Huang, M. H. *In situ* grown Ni phosphate@$Ni_{12}P_5$ nanorod arrays as a unique core–shell architecture: Competitive bifunctional electrocatalysts for urea electrolysis at large current densities. *ACS Sustainable Chem. Eng.* **2020**, *8*, 7463–7471.

[33] Wang, C.; Zhang, L.; Xu, G. C.; Yang, L. F.; Yang, J. H. Construction of unique ternary composite $MCNTs@CoS_x@MoS_2$ with three-dimensional lamellar heterostructure as high-performance bifunctional electrocatalysts for hydrogen evolution and oxygen evolution reactions. *Chem. Eng. J.* **2021**, *417*, 129270.

[34] Wang, Y. F.; Chen, Z.; Han, P.; Du, Y. H.; Gu, Z. X.; Xu, X.; Zheng, G. F. Single-atomic Cu with multiple oxygen vacancies on ceria for electrocatalytic CO_2 reduction to CH_4. *ACS Catal.* **2018**, *8*, 7113–7119.

[35] Liu, S. J.; Zhu, J.; Sun, M.; Ma, Z. X.; Hu, K.; Nakajima, T.; Liu, X. H.; Schmuki, P.; Wang, L. Promoting the hydrogen evolution reaction through oxygen vacancies and phase transformation engineering on layered double hydroxide nanosheets. *J. Mater. Chem. A* **2020**, *8*, 2490–2497.

[36] Shao, Z. Y.; Qi, H.; Wang, X.; Sun, J.; Guo, N. K.; Huang, K. K.; Wang, Q. Boosting oxygen evolution by surface nitrogen doping and oxygen vacancies in hierarchical NiCo/NiCoP hybrid nanocomposite. *Electrochim. Acta* **2019**, *296*, 259–267.

[37] Xu, T. Y.; Jiao, D. X.; Zhang, L.; Zhang, H. Y.; Zheng, L. R.; Singh, D. J.; Zhao, J. X.; Zheng, W. T.; Cui, X. Q. Br-induced P-poor defective nickel phosphide for highly efficient overall water splitting. *Appl. Catal. B: Environ.* **2022**, *316*, 121686.

[38] Lin, Y.; Sun, K. A.; Liu, S. J.; Chen, X. M.; Cheng, Y. S.; Cheong, W. C.; Chen, Z.; Zheng, L. R.; Zhang, J.; Li, X. Y. et al. Construction of CoP/NiCoP nanotadpoles heterojunction interface for wide pH hydrogen evolution electrocatalysis and supercapacitor. *Adv. Energy Mater.* **2019**, *9*, 1901213.

[39] Liu, Y.; Feng, Q. G.; Liu, W.; Li, Q.; Wang, Y. C.; Liu, B.; Zheng, L. R.; Wang, W.; Huang, L.; Chen, L. M. et al. Boosting interfacial charge transfer for alkaline hydrogen evolution via rational interior Se modification. *Nano Energy* **2021**, *81*, 105641.

[40] Chen, L.; Wang, Y. P.; Zhao, X.; Wang, Y. C.; Li, Q.; Wang, Q. C.; Tang, Y. G.; Lei, Y. P. Trimetallic oxyhydroxides as active sites for large-current-density alkaline oxygen evolution and overall water splitting. *J. Mater. Sci. Technol.* **2022**, *110*, 128–135.

[41] Zhang, Y.; Guo, H. R.; Li, X. P.; Du, J.; Ren, W. L.; Song, R. A 3D multi-interface structure of coral-like Fe-Mo-S/Ni_3S_2@NF using for high-efficiency and stable overall water splitting. *Chem. Eng. J.* **2021**, *404*, 126483.

[42] Li, X. Y.; Xiao, L. P.; Zhou, L.; Xu, Q. C.; Weng, J.; Xu, J.; Liu, B. Adaptive bifunctional electrocatalyst of amorphous CoFe oxide@2D black phosphorus for overall water splitting. *Angew. Chem., Int. Ed.* **2020**, *59*, 21106–21113.

[43] Jin, R. X.; Huang, J.; Chen, G. L.; Chen, W.; Ouyang, B.; Chen, D. L.; Kan, E. J.; Zhu, H.; Li, C. R.; Yang, D. Z. et al. Water-sprouted, plasma-enhanced Ni-Co phospho-nitride nanosheets boost electrocatalytic hydrogen and oxygen evolution. *Chem. Eng. J.* **2020**, *402*, 126257.

[44] Liu, W. X.; Yu, L. H.; Yin, R. L.; Xu, X. L.; Feng, J. X.; Jiang, X.; Zheng, D.; Gao, X. L.; Gao, X. B.; Que, W. B. et al. Non-3d metal modulation of a 2D Ni–Co heterostructure array as multifunctional electrocatalyst for portable overall water splitting. *Small* **2020**, *16*, 1906775.

[45] Wang, P. Y.; Zhang, L.; Wang, Z.; Bu, D. C.; Zhan, K.; Yan, Y.; Yang, J. H.; Zhao, B. N and Mn dual-doped cactus-like cobalt oxide nanoarchitecture derived from cobalt carbonate hydroxide as efficient electrocatalysts for oxygen evolution reactions. *J. Colloid Interface Sci.* **2021**, *597*, 361–369.

[46] Yao, N.; Li, P.; Zhou, Z. R.; Meng, R.; Cheng, G. Z.; Luo, W. Nitrogen engineering on 3D dandelion-flower-like CoS_2 for high-performance overall water splitting. *Small* **2019**, *15*, 1901993.

[47] He, J. T.; Liu, F.; Chen, Y. K.; Liu, X. Y.; Zhang, X. L.; Zhao, L. L.; Chang, B.; Wang, J. G.; Liu, H.; Zhou, W. J. Cathode electrochemically reconstructed V-doped CoO nanosheets for enhanced alkaline hydrogen evolution reaction. *Chem. Eng. J.* **2022**, *432*, 134331.

[48] Wang, J.; Hu, J.; Liang, C.; Chang, L. M.; Du, Y. C.; Han, X. J.; Sun, J. M.; Xu, P. Surface reconstruction of phosphorus-doped cobalt molybdate microarrays in electrochemical water splitting. *Chem. Eng. J.* **2022**, *446*, 137094.

[49] Wang, C.; Qi, L. M. Heterostructured inter-doped ruthenium-cobalt oxide hollow nanosheet arrays for highly efficient overall water splitting. *Angew. Chem., Int. Ed.* **2020**, *59*, 17219–17224.

[50] Hu, F.; Zhu, S. L.; Chen, S. M.; Li, Y.; Ma, L.; Wu, T. P.; Zhang, Y.; Wang, C. M.; Liu, C. C.; Yang, X. J. et al. Amorphous metallic NiFeP: A conductive bulk material achieving high activity for oxygen evolution reaction in both alkaline and acidic media. *Adv. Mater.* **2017**, *29*, 1606570.

[51] Li, R. C.; Hu, B. H.; Yu, T. W.; Chen, H. X.; Wang, Y.; Song, S. Q. Insights into correlation among surface–structure–activity of cobalt-derived pre-catalyst for oxygen evolution reaction. *Adv. Sci.* **2020**, *7*, 1902830.

[52] Xue, H. Y.; Meng, A. L.; Zhang, H. Q.; Lin, Y. S.; Li, Z. J.; Wang, C. S. 3D urchin like V-doped CoP *in situ* grown on nickel foam as bifunctional electrocatalyst for efficient overall water-splitting. *Nano Res.* **2021**, *14*, 4173–4181.

[53] Li, A.; Zhang, L.; Wang, F. Z.; Zhang, L.; Li, L.; Chen, H. M.; Wei, Z. D. Rational design of porous Ni-Co-Fe ternary metal phosphides nanobricks as bifunctional electrocatalysts for efficient overall water splitting. *Appl. Catal. B: Environ.* **2022**, *310*, 121353.

[54] Su, H.; Song, S. J.; Li, S. S.; Gao, Y. Q.; Ge, L.; Song, W. Y.; Ma, T. Y.; Liu, J. High-valent bimetal Ni_3S_2/Co_3S_4 induced by Cu doping for bifunctional electrocatalytic water splitting. *Appl. Catal. B: Environ.* **2021**, *293*, 120225.

[55] Zhang, Y. Q.; Liu, H. B.; Ge, R. Y.; Yang, J.; Li, S. A.; Liu, Y.; Feng, L. Y.; Li, Y.; Zhu, M. Y.; Li, W. X. Mo-induced *in-situ* architecture of Ni_xCo_yP/Co_2P heterostructure nano-networks on nickel foam as bifunctional electrocatalysts for overall water splitting. *Sustainable Mater. Techno.* **2022**, *33*, e00461.

[56] Kang, Y.; Wang, S.; Zhu, S. Q.; Gao, H. X.; Hui, K. S.; Yuan, C. Z.; Yin, H.; Bin, F.; Wu, X. L.; Mai, W. J. et al. Iron-modulated nickel cobalt phosphide embedded in carbon to boost power density of hybrid sodium-air battery. *Appl. Catal. B: Environ* **2021**, *285*, 119786.